Tunable wettability of polymer films by partial engulfment of nanoparticles

Weiteng Guo,[1] Chongnan Ye,[1] Gert H. ten Brink,[1] Katja Loos,[1] Vitaly B. Svetovoy,[2] and George Palasantzas[1,*]

[1]*Zernike Institute forAdvanced Materials, University of Groningen, Nijenborgh 4, 9747 AG Groningen, The Netherlands*

[2]*A. N. Frumkin Institute of Physical Chemistry and Electrochemistry, Russian Academy of Sciences, Leninsky Prospect 31 Bld. 4, 119071 Moscow, Russia*

(Received 7 October 2020; accepted 12 January 2021; published 25 January 2021)

A series of poly(methyl methacrylate) (PMMA) surfaces decorated by Cu nanoparticles (NP) with gradually varied morphology were prepared by high-pressure CO_2 treatment at various time spans. Combining the characterizations of transmission electron microscopy (TEM) and atomic force microscopy (AFM), an accurate three-dimensional view of the morphology of the surfaces was presented. Subsequently, the wettability of the surfaces decreases near linearly with the increase of the apparent height of the decorating NPs in both static (static contact angle) and dynamic (contact angle hysteresis) aspects. The observed tendency contradicts to the Wenzel or Cassie-Baxter model and is explained by the contribution of nanomeniscus formed between the decorating NP and the flat substrate. The capillary pressure from this meniscus is negative and results in the increase of the contact angle with the apparent height (H_N) of the Cu NPs decorating the PMMA surface. In addition, the effect of the coverage (C_N) by NPs on the wettability can be explained on the same basis. Our experiment demonstrates the important influence of the nanomeniscus on the wettability, which is usually not taken into account. The results in this work provide a comprehensive understanding of how nanostructure affects the wettability of the decorated surfaces and shed light on how to obtain certain wettability through nanostructuring of the surface morphology.

DOI: 10.1103/PhysRevMaterials.5.015604

I. INTRODUCTION

Currently, relentless efforts have been devoted to creating different types of roughness to enable control of the wettability of surfaces. With high static contact angle (SCA) and low contact angle hysteresis (CAH), the lotus leaf [1] inspired various applications such as, for example, self-cleaning surfaces [2] and low-friction surfaces for fluid flow [3]. Unlike the lotus leaf, some rose petals [4], scallions, and garlic exhibit superhydrophobicity with high CAH [4–6], inspiring applications in fields such as droplet transportation [7] and energy harvesting [8]. Although the wetting behavior of lotus leaflike surfaces and rose-petal-like surfaces differ a lot with each other, an important path to realizing the certain wettability is building up the microstructure of the surfaces. Therefore, understanding the relationship between wettability and detailed surface morphology is important for designing surfaces with certain wettability for various applications.

Much effort has been made toward understanding and describing roughness and wettability, and the models of Wenzel [9] and Cassie-Baxter [10] are the two most widely used ones. In the Wenzel theory, the testing droplet wets the cavities of the surface, enlarging the interaction area with the liquid droplet. And the apparent SCA θ_W in terms of the Wenzel model is given by the expression $\cos\theta_W = r\cos\theta_Y$ [9], where $r = A_r/A_p$ is the roughness factor with A_r the actual rough surface area and A_p the projected surface area on the average surface plane. However, in several cases, e.g., the lotus effect, [11–13] there are air pockets trapped between the solid surface and the testing droplet. This case is described by the Cassie-Baxter model, where the apparent SCA θ_{CB} is given by the expression $\cos\theta_{CB} = f\cos\theta_y + (f-1)$, [10], where f is the fraction of the solid surface area wetted by the liquid.

Although the two well-known models have enabled the explanation of the wettability of surfaces with various types of morphology, several other studies have demonstrated complex cases of surface wettability, where the Wenzel and Cassie-Baxter models could not explain the experimental data. Taking the air-liquid interface on a solid as a one-dimensional system, Pease [14] emphasized that the SCA is the result of an equilibrium position that the three-phase contact line (TPL) could reach. This perspective was supported by experiments, where the pinning effect of the contact line was observed on microstructured [15] and nano-structured surfaces [16], and extensively discussed and summarized by Gao and McCarthy [17]. These works illustrated that the reason why the Wenzel model failed to predict the SCA of microstructured surfaces was that a thermodynamic description could not account for contact line pinning. Therefore, the local equilibrium of the TPL is critical to describe the relationship of the wettability and geometrical features (roughness), inspiring more studies to explore the effects of macrosized or nanosized decorations on wettability. Using microsized square pillars with various sizes and concentrations, Forsberg *et al.* [18] revealed the microscopic details of the contact line pinning behavior, and bridged the relationship between the wettability and the varied microsized decorations. Furthermore, the contact line pinning

*Corresponding author: g.palasantzas@rug.nl

behavior could be analyzed to a nanometer scale, [16,19] where the mechanism of pinning at a nanometric scale might be attributed to the nanomeniscus formed between the substrate and the nanoscale decoration [20]. Also, simulations of the contact line pinning effect on nanoscale textured surfaces [21] and the pinning effect of a single nanoparticle [22] were conducted to give a deep understanding of the relationship between wettability and nanostructure. However, experimental investigations taking into account nanoscale defects are still limited, because such studies are faced with the difficulty of obtaining and characterizing rough surfaces having a controlled morphology of the nanostructure. Therefore, the goal of the present work is to create a series of surfaces with gradually varied nanostructure to understand the influence of nanometric decorations on the wetting properties of a solid surface.

In this framework, nanoparticles (NPs) provide an ideal option to create nanostructured surfaces and achieve certain wettability, e.g., TiO_2 NP painting [23]. or even more directly, e.g., Cu NP deposition by a high-pressure magnetron sputtering system where the production and decoration process can be accomplished in one step [24]. Moreover, the high-pressure magnetron sputtering can offer homogeneously distributed Cu NPs onto flat substrates without introducing additional chemical ligand [24,25], which made it an ideal candidate to provide nanostructured decoration for wetting research. Also, Teichroeb *et al.* [26] studied the embedding of gold nanoparticles into the surface of polystyrene (PS) to probe the viscoelasticity of polymer surfaces. Subsequently, Tan *et al.* [27] reported the controlled thermally assisted particle embedding of surface deposited silica NPs at the surface of poly(methyl methacrylate) (PMMA) polymer films. Particle embedding was controlled by varying the temperature and time of the thermal treatment, and similar results were obtained for surface-modified silica NPs in PMMA and poly(methyl methacrylate-co-methacrylic acid) films [28]. As an alternative to thermal annealing, Lee *et al.* [29] and Yang *et al.* [30] reported the embedding of gold NPs in PS films via CO_2 saturation of the polymer substrate at relatively low temperatures, because a CO_2 saturated PS surface exhibits an increased polymer mobility, allowing the particles to sink into the surface. Furthermore, Liu *et al.* [31] gave extensive experimental results and theoretical analysis of the high-pressure CO_2 assisted engulfment of NPs on PMMA, proving the high-pressure CO_2 a reliable method to conduct NP engulfment on polymer films. Therefore, we have gathered ideal candidates of nanostructured decoration (magnetron sputtered Cu NPs) and substrate (PMMA) to design nanostructured surfaces for wetting research.

Here we used the high-pressure CO_2 assisted NP engulfment technique, and designed a series of samples with Cu NPs decorated PMMA surfaces with gradually varied apparent height of NPs by controlling the time span of high-pressure CO_2 treatment. Taking advantage of the superior lateral resolution of transmission electron microscopy (TEM) and vertical resolution of atomic force microscopy (AFM), an accurate three-dimensional view of the morphology of the surfaces was presented. Subsequently, wetting measurements of SCA as well as advancing contact angle (ACA) and receding contact angle (RCA) were conducted on the surfaces with

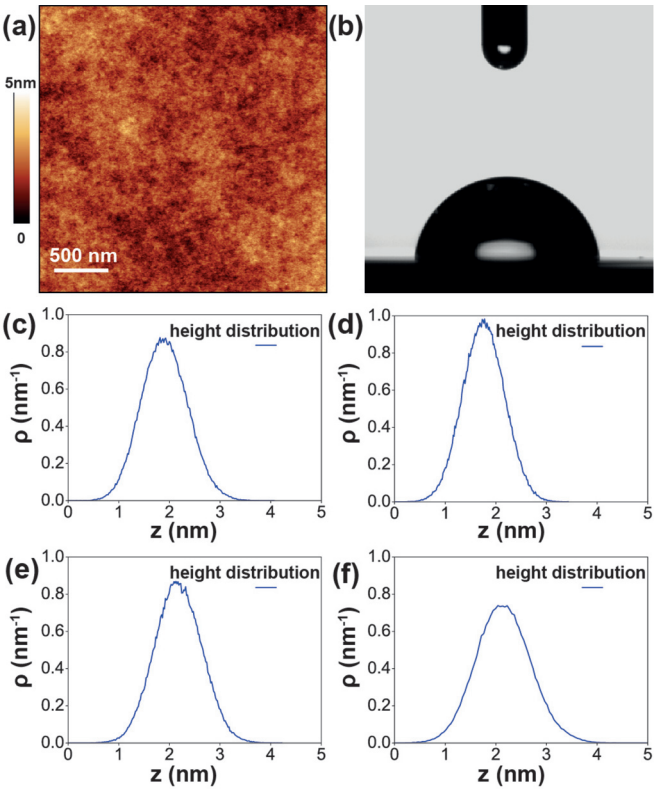

FIG. 1. Atomic force microscopy (AFM) and wettability studies of the PMMA surfaces with various exposure times to high-pressure CO_2 treatments (58 bar). (a) AFM image of the PMMA without high-pressure CO_2 treatment with scan area of $3 \times 3\,\mu m^2$. (b) SCA of the PMMA without high-pressure CO_2 treatment. (c)–(f) Height distributions of PMMA samples with 0 min (no treatment), 5-, 30-, and 90-min high-pressure CO_2 treatments, respectively, derived from AFM topography measurements with scan area of $3 \times 3\,\mu m^2$.

controlled nanoscale morphology. Finally, a model involving the wettability contribution of the nanomeniscus formed between the decorating NP and the flat substrate was proposed to describe the relationship between the wettability and apparent height (H_N) of the Cu NP decorating PMMA surfaces.

II. EXPERIMENTAL RESULTS AND DISCUSSION

Here we will present our main experimental results and discussion about them, while details about the preparation methods and characterization techniques are given in the Appendix.

A. Wettability of PMMA films

The PMMA films were made using the same method as in the work of Liu *et al.* [31] The thickness of the PMMA films was measured to be about 50 μm [31], which is sufficiently thick to be taken as a bulk in the wetting study in this work. Additionally, the PMMA films on silica wafers were very smooth [see Fig. 1(a)], showing them as very suitable substrates for the current wetting research. In addition, the wetting measurements of the different PMMA films showed stable wettability [with SCA 81.5 $\pm$ 0.5 ° in Fig. 1(b), and

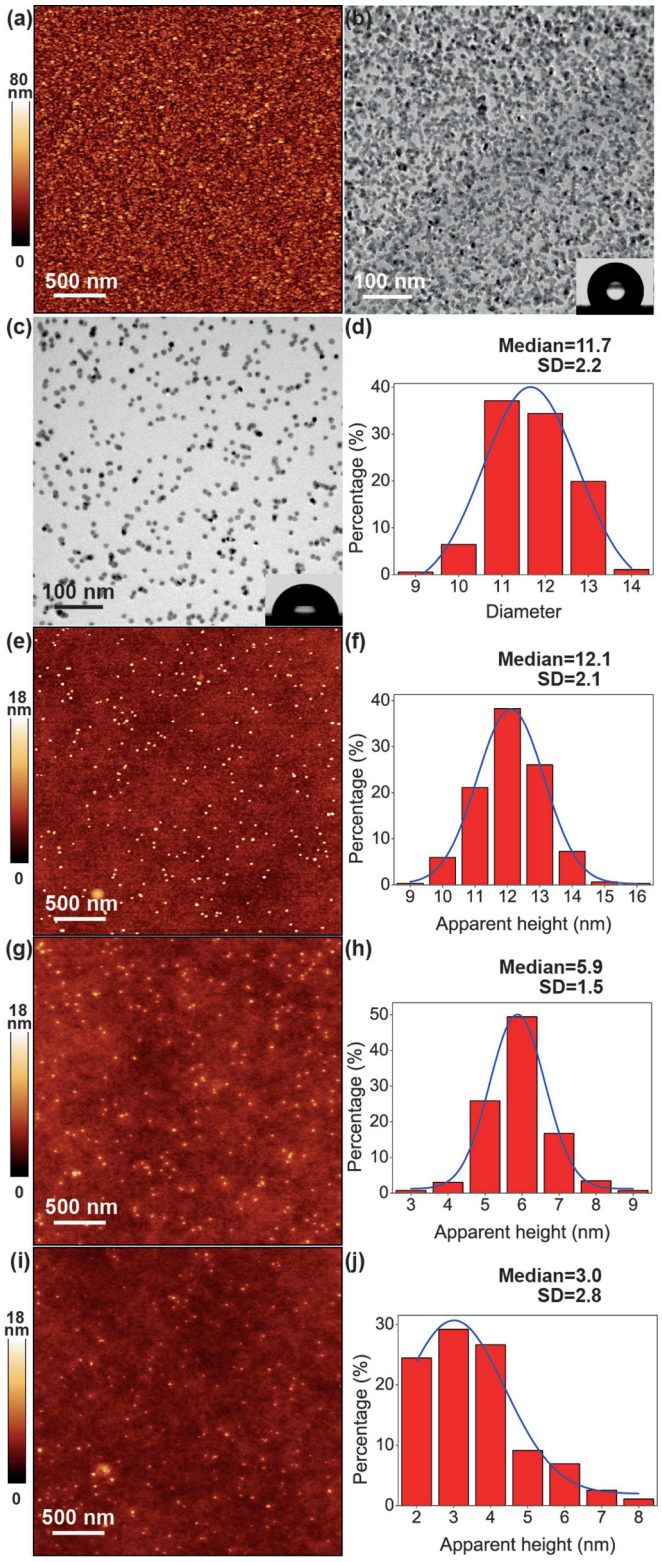

FIG. 2. Morphology and wetting studies of the high (64%)/low (12%)-C_N samples. (a) AFM image of the high (64%)-C_N sample with scan area of $3 \times 3\,\mu m^2$. (b) TEM image of the Cu NPs deposited on a TEM grid simultaneously with the NPs deposited on the PMMA films including also the SCA (bottom right corner) for the high (64%)-C_N Cu NPs/PMMA sample. (c) TEM image of Cu NPs deposited on a TEM grid simultaneously with the NPs deposited on the PMMM films with the SCA indicated (in the bottom right corner) of the low (12%)-C_N Cu NPs/PMMA sample. (d) Distribution of the diameter of NPs measured in (c). (e), (g), (i) AFM images (scan area: $3 \times 3\,\mu m^2$) of low (12%)-C_N Cu NPs/PMMA samples with 0 min (no treatment), 30- and 90-min high-pressure CO_2 treatments, respectively. (f), (h), (j) Apparent height distributions of the monodispersed NPs measured in (e), (g), (i), respectively.

ACA 83 °, RCA 70.5 ± 0.5 ° for dynamic wettability]. Besides the stable wettability, also the morphology of the PMMA films did not show any significant variation. On behalf of checking the effect of the high-pressure CO_2 treatment on the morphology and wettability of PMMA films, we put an extra PMMA film together with the NPs/PMMA samples during each high-pressure CO_2 treatment. As a result, there was no evident variation among the wettability and the height distributions [see Figs. 1(c)–1(f)] of the PMMA surfaces after high-pressure CO_2 treatments with various time spans.

B. Effect of Cu NPs on wettability of PMMA films

In our previous study [20], a hypothesis has been formulated that the increase of the SCA of a surface could be generated by the nanomeniscus, whose existence has been proved by experiments [32–34] and theoretical analysis [35–37], formed between the substrate and the decorating NPs. Subsequently, it is reasonable to assume that the effect would become weaker when the NPs are partially submerged into the substrate, and the untreated samples have to demonstrate the highest SCA. Therefore, the first step to check the hypothesis is to allow the Cu NPs to induce a difference in the wettability of the PMMA and then measure the variation of the wettability after high-pressure CO_2 treatments. Knowing that the surfaces with higher NP coverage C_N (the ratio of the area covered with NPs with respect to the overall area as determined by the TEM images, which is the same definition used in our previous works [20,24]) tend to show large SCA [24], we started from the preparation of high-C_N Cu NPs/PMMA samples. The morphology as well as the SCA of the Cu NPs decorated PMMA samples are shown in Figs. 2(a) and 2(b). The C_N was measured to be about 64%, and the SCA of the PMMA film has experienced a significant increase from 81.5 ± 0.5 ° [see Fig. 1(a)] to 122 ± 1 ° [see Fig. 2(b)] after the deposition of Cu NPs. However, the in-plane resolution (see Supplemental Material for details [38]) of the AFM images is not good enough to distinguish two NPs close to each other [39] because of the tip shape effect [40,41]. When the C_N is too high, i.e., 64% in this case, the individual NPs would be too close to each other for the AFM tip to distinguish them. As a result, the AFM image would appear to be totally "covered" by NPs, and apparent heights of the individual NPs are hardly accessible for so high C_N sample, though the AFM vertical resolution is outstanding [42]. Therefore, lower C_N PMMA films are necessary for obtaining the apparent heights of the individual decorating NPs.

C. Partial NP engulfment in PMMA

Since the samples with high C_N were not suitable for height measurement of the individual decorating NPs, low-C_N Cu NP/PMMA samples were prepared, offering sufficient

flexibility for the size analysis of the Cu NPs. Since an NP could completely sink into PMMA with high-pressure CO_2 treatment when its diameter is below 12 nm [31], the deposition parameters of the sputtering system for Cu NPs were optimized to obtain NPs with a diameter of approximately 12 nm (the method for controlling the diameter of Cu NPs was discussed in our previous work [25]) so that one can achieve various degrees of engulfment in the PMMA film. The coverage of the samples was measured to be about 12% in Fig. 2(c), which offers NPs with good monodispersity for dimensional measurements. In fact, image analysis with the Image-Pro Plus v6.0 software yielded the distribution of the diameter (D_N) of the NPs as it is shown in Fig. 2(d).The median value of D_N was 11.7 nm by fitting with a Gaussian function (more than 220 individual isolated NPs were measured), while the standard deviation (*SD*) was 2.2 nm, indicating a good fit by the Gaussian model as well.

The SCAs of the low (12%)-C_N samples were measured to be approximately 81 °, showing no noticeable difference in wettability from bare PMMA films (81.5 ± 0.5 °, Fig. 1). However, the good NP monodispersity makes the low C_N samples suitable candidates for AFM analysis. The apparent heights (H_N) of the individual NPs (see Supplemental Material [38] for details) on the low (12%)-C_N samples before high-pressure CO_2 treatment were derived from Fig. 2(e) and summarized in Fig. 2(f). The median of H_N (for meaningful statistics the value of H_N for 270 individual isolated NPs were measured) was evaluated as 12.1 nm by fitting with the Gaussian function, while the obtained *SD* was 2.1 nm indicating that the fit of the data by the Gaussian function is good. Moreover, the median of H_N (12.1 nm) agrees well with the median of D_N [11.7 nm shown in Fig. 2(d)], which was measured in the TEM image [Fig. 2(c)], indicating the absence of NP engulfment before high-pressure CO_2 treatment. In addition, the agreement between the TEM and AFM studies represent a consistency check of the lateral/vertical resolution of the TEM/AFM images. The latter could allow the reconstruction of an accurate three-dimensional view of the samples. Additionally, no obvious deposition-caused damage was observed when comparing Fig. 1(a) and the NPs-uncovered areas in Fig. 2(e), indicating the magnetron sputtering system used in this work would not do damage to the PMMA films.

Subsequently, high-pressure CO_2 treatments of 30 and 90 min were conducted to the low-C_N samples, respectively. The corresponding AFM images are shown in Fig. 2(g) and Fig. 2(i), respectively. Then the height H_N of 270 isolated individual NPs were measured, and the results were summarized in Figs. 2(h) and 2(j). The median of H_N of the 30-min CO_2 treated sample was evaluated to be 5.9 nm by the Gaussian fitting with an *SD* of 1.5 nm indicating a good fit. However, for the 90-min CO_2 treated sample, the median of H_N was evaluated to be 3.0 nm with a large *SD* of 2.8 nm. The latter can be understood by the observed asymmetry of the distribution for H_N in Fig. 2(j), which may be caused by the uncertainty of measuring the NPs with H_N lower than 2 nm in the AFM image. Comparing the results in Figs. 2(e)–2(j), it can be concluded that the Cu NPs are in metastable mechanical state and gradually sink into PMMA films during the high-pressure CO_2 treatment, where the NPs will undergo more engulfment with more extended high-pressure CO_2 treatment [31].

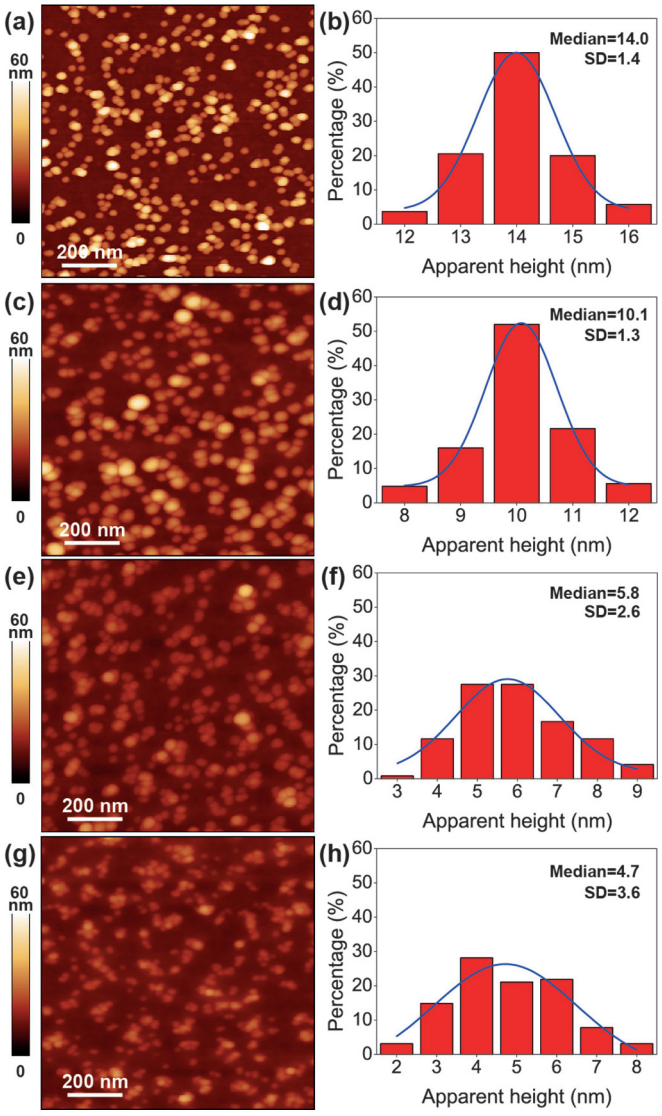

FIG. 3. Morphology studies of the "intermediate" (37%)-C_N Cu NPs/PMMA samples. (a), (c), (e), (g) AFM images (scan area: 1 × 1 μm^2) of the Cu NPs/PMMA samples with 0 min (no treatment), 5 min, 30 min, and 90 min high-pressure CO_2 treatments, respectively. (b), (d), (f), (h) Apparent height distributions of monodispersed NPs measured in (a), (c), (e), (g), respectively.

Additionally, the number density as well as the distribution of decorating NPs did not vary a lot in the AFM images shown in Figs. 2(e), 2(g), 2(i), indicating that all the individual NPs sank uniformly during the high-pressure CO_2 treatments. Therefore, the high-pressure CO_2 treatment used in this work is an ideal method for controlling the H_N of NPs on PMMA films and creating a series of Cu NPs/PMMA samples with comparable morphologies.

D. Wettability vs NP engulfment into PMMA

The Cu NPs/PMMA samples with the "intermediate"-C_N (37%) were studied extensively. The morphology studies of the NP engulfment into PMMA and the wettability studies of the relevant samples are shown in Figs. 3 and 4, respectively. Besides the AFM images in Figs. 3(a), 3(c), 3(e), 3(g), the

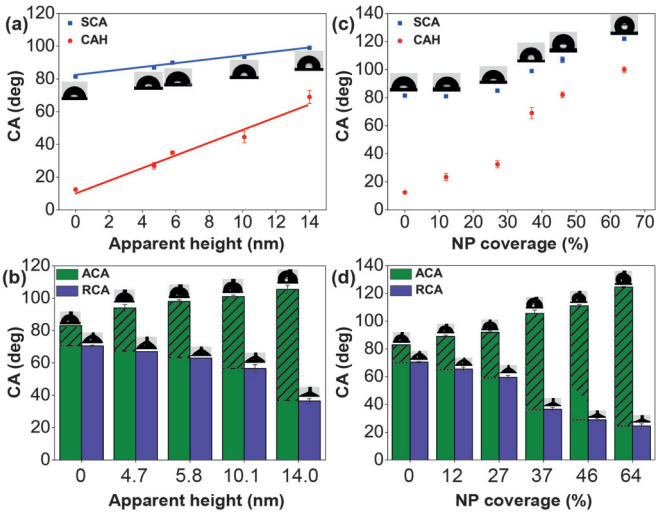

FIG. 4. Wetting studies of the "intermediate" (37%)-C_N Cu NPs/PMMA samples with various medians of H_N, and the Cu NPs/PMMA samples with various C_N before high-pressure treatments. (a) SCAs and CAH of the "intermediate" (37%)-C_N samples with various medians of H_N, where the square (blue) spots refer to the SCAs, and the circle (red) ones refer to the CAH. (b) ACAs and RCAs of the "intermediate" (37%)-C_N samples with various medians of H_N, where the green bars refer to the ACAs and the purple bars to the RCAs, and the dashed areas in the green bars refer to the CAH of the samples.(c) SCAs and CAH of the samples with various C_N coverages, where the square (blue) spots refer to the SCAs and the circle (red) ones to the CAH. (d) ACAs and RCAs of the samples, where the green bars refer to the ACAs and the purples ones to the RCAs, as well as the dashed areas in the green bars refer to the CAH.

height H_N of the isolated NPs were also measured in two additional AFM images (see Supplemental Material [38] for details) derived from each sample to improve statistics. In fact, the H_N of more than 120 individual isolated particles were analyzed for each H_N distribution and shown in Figs. 3(b), 3(d), 3(f), 3(h). The distribution of H_N in the "intermediate" (37%)-C_N sample before any high-pressure CO_2 treatment was obtained from Fig. 3(a) and shown in Fig. 3(b). The median of H_N was evaluated to be 14.0 nm (by fitting with a Gaussian function with $SD = 1.4$ nm). Additionally, the median of D_N was evaluated to be 13.2 nm (see Supplemental Material [38] for details). Similar to the agreement between the results in Figs. 2(f) and 2(d), the median of H_N (14.0 nm) agrees well with the median of D_N (13.2 nm) indicating the absence of any NP engulfment before the high-pressure CO_2 treatment, and the satisfactory accuracy of the lateral/vertical resolution of the TEM/AFM images.

Subsequently, three "intermediate" (37%)-C_N samples were treated separately by high-pressure CO_2 for 5, 30, and 90 min, respectively. The AFM images and distributions of H_N are shown in Fig. 3. All the distributions of H_N were fitted by the Gaussian function, and the medians of H_N for the 5-, 30-, and 90-min CO_2 treated samples were 10.1 nm ($SD = 1.3$ nm), 5.8 nm ($SD = 2.6$ nm), and 4.7 nm ($SD = 3.6$ nm), respectively. The results in Fig. 3 are similar to the ones in Figs. 2(e)–2(j), reconfirming that the high-pressure CO_2 treatment used in this work is a reliable way for NP engulfment into PMMA.

TABLE I. Wettability data of the "intermediate" (37%)-NP coverage Cu NPs/PMMA samples with various H_N, and the Cu NPs/PMMA samples with various C_N prior to high-pressure CO_2 treatments.

H_N(nm)	SCA(deg)	ACA(deg)	RCA(deg)	CAH(deg)
0	81.5 ± 0.5	83	70.5 ± 0.5	12.5 ± 0.5
4.7	87 ± 1	94 ± 2	67	27 ± 2
5.8	90	98 ± 1	63	35 ± 1
10.1	93.5 ± 0.5	101 ± 1	56.5 ± 2.5	44.5 ± 3.5
14.0	99	105.5 ± 2.5	36.5 ± 1.5	69 ± 4
C_N(%)				
0	81.5 ± 0.5	83	70.5 ± 0.5	12.5 ± 0.5
12	81	89 ± 1	65.5 ± 1.5	23.5 ± 2.5
27	85 ± 1	98 ± 1	59.5 ± 1.5	32.5 ± 2.5
37	99	101 ± 1	36.5 ± 1.5	69 ± 4
46	107 ± 2	105.5 ± 2.5	29 ± 1	82 ± 2
64	122 ± 1	124.5 ± 0.5	24.5 ± 1.5	100 ± 2

Subsequently, the wettability of the "intermediate" (37%)-C_N samples was measured and summarized in Table I and Figs. 4(a) and 4(b). The square (blue) spots in Fig. 4(a) show the evolution of the SCAs starting from 81.5 ± 0.5° (bare PMMA film) to 99° (NPs/PMMA without high-pressure CO_2 treatment). The SCA appears to increase almost linearly as a function of medians of H_N, where $\chi^2 = 0.99$ with linear regression shown in Fig. 4(a) (χ^2 is the coefficient of determination defined as $\chi^2 = 1 - SS_{RES}/SS_{TOT}$). Considering the fact that the high-pressure CO_2 treatment changed neither the morphology nor the wettability of the PMMA films (see Fig. 1), the SCA of the Cu NPs/PMMA samples can only be associated to the variation of H_N of the decorating NPs.

Furthermore, the ACAs and RCAs of the samples were measured to explore the dynamic wettability of the samples, and the results are summarized in Fig. 4(b). In general, the results of ACA show a similar tendency to the results of SCA. Specifically, the difference between bare PMMA film and the 90-min high-pressure CO_2 treated sample for the ACA (~11°) was more significant than the one in SCA (~5.5°), indicating that the decorating NPs might play a more important role in dynamic wettability as compared with the static one. Moreover, this phenomenon was more dramatic for the results of RCA. In general, the RCAs of the samples showed an inverse tendency as compared with that of ACAs and SCAs, while the "rate" of variation is higher compared with the ones of the ACA and SCA.

According to the definition of the CAH $\theta_H = \theta_A - \theta_R$ (with θ_A the ACA and θ_R the RCA) [43], the θ_H is marked as the dashed areas in the (green) bars of Fig. 4(b), while it is shown as the circular (red) spots in Fig. 4(a). Similar to the dependence of SCA from H_N, the relationship between the CAH and H_N also followed a near-linear behavior with $\chi^2 = 0.97$ by linear regression. However, the slope of the profile of CAH-H_N is larger than the one of SCA-H_N, suggesting again that the dynamic wettability is more "sensitive" to decorating NPs than the static one.

In addition, we have also summarized the SCAs derived from the Cu NPs/PMMA samples with various C_N values (see Table I), as it is shown by the square (blue) spots in Fig. 4(c). The profile starts from the PMMA film with an SCA of 81.5 ± 0.5 °, undergoing no notable change before the SCA of 37%-C_N sample (99 °). Subsequently, the SCA increased in an almost linear manner. Aiming to provide more supporting information by Fig. 4(d), the ACAs and RCAs were also measured from the samples and summarized in Table I. In detail, the difference between bare PMMA film and the 12%-C_N sample in ACA (∼6 °) was more significant than the one in SCA (∼-0.5 °), reconfirming the conclusion derived from the results in Figs. 4(a) and 4(b) that the decorating NPs likely play more important role in the dynamic than the static wettability.

Again, the RCAs of the samples showed an inverse behavior compared with the one of the ACAs or SCAs. Notably, the RCA displayed a sudden drop between the 27%-C_N and the 37%-C_N sample with a difference of 23 °. Also, the results of CAH are marked as the dashed areas in Fig. 4(d). In detail, the gap between the 27%-C_N sample and the 37%-C_N sample in CAH (∼36.5 °) is much larger than the one in SCA (14 °). On the one hand, the dynamic wettability analysis reconfirmed that the 37%-C_N was located near the critical point of the NP coverage, where the wettability changed strongly enough to indicate that this sample was a good candidate for the subsequent wettability-NP engulfment investigation. On the other hand, the comparison between the results for CAH and SCA supported the suggestion obtained from Figs. 4(a) and 4(b) that the dynamic wettability is more "sensitive" to the decorating NPs than the static one.

III. NANOMENISCUS EFFECT ON WETTABILITY

Neither of the two widely-used Wenzel [9] and Cassie-Baxter [10] models is suitable for analyzing the wettability of the Cu NP decorated PMMA surfaces. On the one hand, the materials used in this work are relatively hydrophilic with similar contact angles (81.5 ± 0.5 ° for PMMA as the substrate material and 79 ° for Cu [20] as the NP material), which makes impossible to generate hydrophobicity within the Wenzel model. On the other hand, the Cu NPs decorated PMMA surfaces were not in the Cassie-Baxter state, because the measured large contact angle hysteresis [see Figs. 4(a) and 4(c)] indicates strong adhesion force between the water meniscus and the tested surface. A similar situation for a surface decorated by NP was discussed previously [20]. It was proposed that the paradox can be resolved by taking into account the formation of a nanomeniscus when liquid wets a spherical particle on a flat surface. This concave nanomeniscus shown schematically in Fig. 5(a) will give a negative contribution to SCA, increasing the effective contact angle of the decorated surface.

Let θ_S be the SCA of the substrate and θ_N is that for the NP material. In the Wenzel model, the effective SCA can be calculated according to the relation

$$\cos\theta_W = f_S \cos\theta_S + f_N \cos\theta_N, \tag{1}$$

where f_S and f_N are the ratios of the true area of the solid surface to the apparent area for the substrate and NP, respectively.

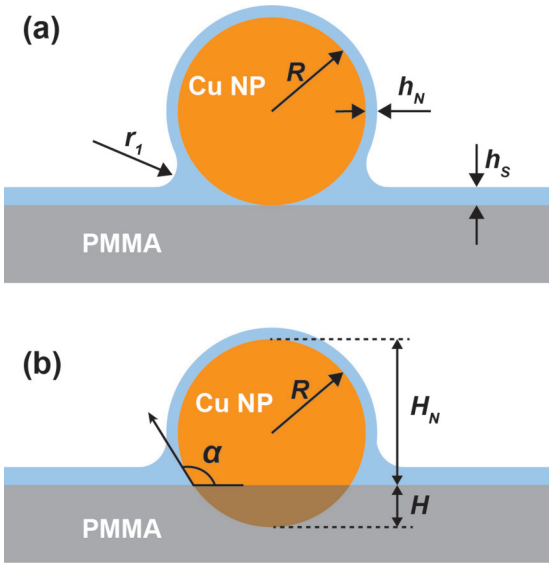

FIG. 5. Schematics for evaluation of nanomeniscus on the wettability of the Cu NP decorated PMMA films. (a) The configuration used to calculate contact angle with Eq. (4): R is the radius of the NP, r_1 is the negative radius of curvature, r_2 (not shown) is the positive radius of curvature in the orthogonal direction to the plane, h_1 is the thickness of wetting film on the substrate, h_2 is the thickness of wetting film on the NPs. (b) The schematic of partial NP engulfment into the PMMA film: H is the depth of the Cu NP submerged into PMMA, H_N is the apparent height of the NP, and α is the angle between the baseline of PMMA and the tangent of the NP from the sectional view.

For a sphere of radius R submerged to the substrate to a depth H these ratios are

$$f_S = 1 - C_N \frac{H(2R-H)}{R^2}, \quad f_N = C_N \frac{2(2R-H)}{R}, \tag{2}$$

where C_N is the surface coverage by the NPs (more details for the derivation of Eq. (2) is seen in Supplemental Material [38]). The contact angle on the flat substrate is defined by the Derjaguin equation [44,45]

$$\cos\theta_S = 1 + \frac{1}{\gamma}\int_{h_S}^{\infty} \Pi_S(h)dh + \frac{h_S}{\gamma}\Pi(h_S). \tag{3}$$

In Eq. (3) $\gamma = \gamma_{lv}$ is the surface tension of the liquid, and h_S is the equilibrium thickness of the wetting film and $\Pi_S(h)$ is the disjoining pressure on the substrate. For macroscopic liquid volumes the capillary pressure $|P_c| \sim \gamma/\mathcal{R}$ is small, where $\mathcal{R}$ is a macroscopic radius of curvature of the meniscus. In this case, the last term in Eq. (3) is small $h_S/\mathcal{R} \ll 1$ since h_S is in the nanometer range. For this reason, we neglected the small term $h_S\Pi_S(h_S)/\gamma$ in Eq. (3) [46]. If the wetting film is thin in comparison with the size of NP $h \ll R$ and the particle is isolated, one could write a similar expression for $\cos\theta_N$ just changing $\Pi_S \to \Pi_N$ and $h_S \to h_N$. However, the nanomeniscus that is formed due to contact of the particle and substrate also gives a contribution to the contact angle and $\cos\theta_N$ can be presented as [20]

$$\cos\theta_N = 1 + \frac{1}{\gamma}\int_{h_N}^{\infty} \Pi_N(h)dh - \int_{h_2}^{\infty}\left(\frac{1}{r_1} - \frac{1}{r_2}\right)dh, \tag{4}$$

where r_1 is the negative radius of curvature [shown in Fig. 5(a)], and r_2 (not shown) is the positive radius of curvature in the orthogonal direction to the plane. These radii always have different signs and obey the condition $r_1 \ll r_2$. This condition guarantees that the contribution of the meniscus is always reducing $\cos\theta_N$. Following the procedure described in the work of Boinovich *et al.* [47], in principle, one can take into account the effects of the order h/R.

In addition, there were some clusters formed by several individual spherical NPs on the samples shown in Figs. S3(a), S3(c), and S3(e). Then the clusters could be taken as "lager NPs" with varied morphology. Subsequently, the shape of the nanomeniscus formed between the cluster and the substrate would change simultaneously. The curvature radius r_1 and r_2 in Eq. (4) would be lager compared with the situation of an individual NP. However, the increase of r_1 will be more significant than that of r_2, because the morphology of the clusters tends to be disclike. As a result, the $\cos\theta_N$ calculated by Eq. (4) would become larger, leading to a lower CA compared with the one of the situations we would apply in the following analysis where all the NPs would disperse perfectly.

Let us denote the last term in Eq. (4) as

$$\Delta(\cos\theta_N) = -\int_{h_2}^{\infty}\left(\frac{1}{r_1}-\frac{1}{r_2}\right)dh. \tag{5}$$

It is responsible for the transition to hydrophobicity, but its direct evaluation is not a simple task. This term cannot be expressed only via the disjoining pressures $\Pi_S(h)$ and $\Pi_N(h)$ in the liquid films on the substrate and on the particle, respectively, because near the apex of the meniscus, a significant contribution comes from the interaction between these films. Moreover, pressure in the liquid gets a nondiagonal tensorial structure that influences the mechanical equilibrium [48]. The equation of mechanical equilibrium in these conditions has been deduced [49], but practically it can be used only for a few simple problems. While we have no a reliable way to estimate $\Delta(\cos\theta_N)$ it is possible to extract some information from the experimental data.

The observed linear dependence of the SCA on the apparent height $2R-H$ suggests that $\Delta(\cos\theta_N)$ is a quadratic function of the parameter $x = H/R$. It is clear from the fact that according to Eqs. (1) and (2) $\cos\theta_W$ is quadratic in x. To cancel the quadratic term $\Delta(\cos\theta_N)$ also has to include the term proportional to x^2. The best linear fit of the data for $\cos\theta_W$ gives $\Delta(\cos\theta_N) = -(0.3955 - 0.0728x + 0.0006x^2)$. As obvious from Fig. 5 the curvature radius r_1 increases when the particle submerges deeper. When the particle sunk completely, this radius has to be infinite and $\Delta(\cos\theta_N) = 0$. The best fit gives $\Delta(\cos\theta_N) = -(0.3955 - 0.0728x + 0.0006x^2)$. Therefore, it is expected that $\Delta(\cos\theta_N)$ has to disappear with the apparent height at $x = 2$. This is not the case, and we have to include explicitly the zero at $x = 2$ in the function $\Delta(\cos\theta_N)$. The behavior of this function at $x \to 2$ follows from a simple analysis. For $x > 1$ the angle α [formed by the plane of the substrate and the tangent plane of the NP, which also passes through the intersection point of the substrate and the NP as it is shown in Fig. 5(b)] at the base of the submerged spherical particle is $\alpha = \frac{\pi}{2} - \sin^{-1}(x-1)$. In the limit $x \to 2$, it behaves as $\alpha \to \sqrt{2(2-x)}$. In this limit, the same behavior is expected for $\Delta(\cos\theta_N)$ that is why at arbitrary x we are looking at the function with the form

$$\Delta(\cos\theta_N) = -(a_0 + a_1x + a_2x^2)\sqrt{1-x/2}\ (0 \leqslant x \leqslant 2). \tag{6}$$

The best fit of the SCA data in Fig. 4(a) gives $a_0 = 0.3955$, $a_1 = 0.0261$, $a_2 = 0.0195$. The function (6) is shown in Fig. 6(a). It decreases nearly linear with the apparent height, but at a height below 4 nm, it is going to zero quickly. Figure 6(b) shows the experimental data (red circles), the linear fit of the data $\theta_W = 81.70 + 1.228x$ (red dashed line), and the function that corresponds to Eq. (1) with $\Delta(\cos\theta_N)$ given by Eq. (6) (blue solid curve). One can see that the solid curve describes the data as well as the linear fit.

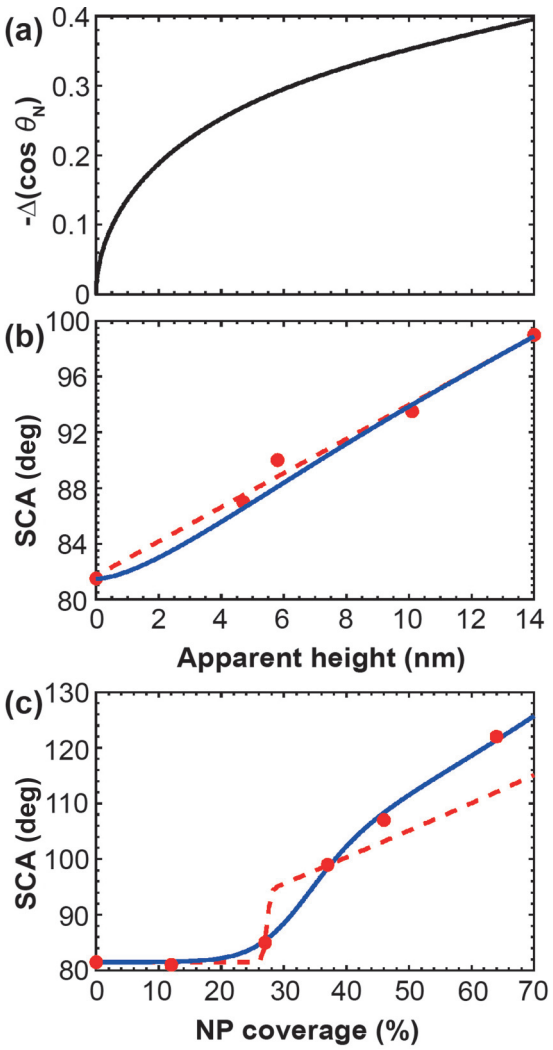

FIG. 6. Relationships between the wettability and morphology of Cu NP decorated PMMA surfaces. (a) The relationship between $\Delta(\cos\theta_N)$ and H_N fitted by Eq. (6). (b) The relationship between SCA and H_N, showing the experimental data (red circles), the linear fit (red dashed line), and the function that corresponds to Eq. (1) with $\Delta(\cos\theta_N)$ given by Eq. (6) (blue solid line). (c) The relationship between SCA and C_N, showing the experimental data (red circles), the best fit according to Eq. (8) (red dashed line), and the best fit by introducing a factor κ (which is positively correlated with the average number of the NP layer on the substrate) into Eq. (8) (blue solid line).

Additionally, the SCA also increases with the increase of C_N [see Fig. 4(c)]. Unlike the SCA-H_N [see Fig. 4(a)], which shows a near-linear relationship, there is an obvious threshold of C_N which "divide" the SCA-C_N profile into two near-linear parts [see Fig. 4(c)]. Therefore, more effort should be made to explore this threshold and describe the SCA-C_N relationship. Although the Wenzel model (1) does not predict the threshold, it is clear that it has to exist since one particle on a large area cannot influence the contact angle. Above the threshold $\cos\theta_W$ behaves linearly with the coverage. Modeling the threshold with a smooth transition, we look for the C_N dependence in the form

$$\cos\theta_W = \cos\theta_S + \frac{a(x)}{2}\left(1 + \tanh\frac{C_N - C_N^0}{\Delta C_N}\right)C_N, \quad (7)$$

where C_N^0 is the position of the threshold and ΔC_N is its width. The amplitude $a(x)$ depending on the parameter x is equal

$$a(x) = (2 - x)[-x\cos\theta_S + 2\cos\theta_N + 2\Delta(\cos\theta_N)]. \quad (8)$$

To compare this dependence with the data in Fig. 4(c) we take $x = 0$ that gives $a(0) = 4(\cos\theta_N - 0.3955)$. For this case the best fit of the data is shown in Fig. 4(c) by the red dashed line. It can be seen that such a dependence fails to describe the data at high coverage. One would expect that above the threshold, the coverage is not reduced exactly to a monolayer of NPs. If we allow the amplitude $a(0)$ to be augmented by a factor κ, then the data are well described by the dependence (7) as shown by the blue solid line. The parameters corresponding to the best fit are $\kappa = 1.278$, $C_N^0 = 0.3202$, $\Delta C_N = 0.0868$. They correspond to the average distance between particles at the threshold equal $3.1R$. It means that any additional particle will form the second layer that justifies the value of κ larger than 1. In addition, the CAH data of the Cu NP decorated PMMA surfaces in Figs. 4(a) and 4(c) showed a similar tendency as the SCAs of the relevant samples, which agreed with the theoretical model in the aspect of dynamic wettability.

IV. CONCLUSIONS

Using the technique of high-pressure Co_2 assisted NP engulfment, a series of Cu NP decorated PMMA surfaces with gradually varied nanostructured morphology were prepared by varying the time span of the high-pressure CO_2 treatment. Combining the characterization of transmission electron microscopy (TEM) and atomic force microscopy (AFM), an accurate three-dimensional view of the morphology of the surfaces was presented. Subsequently, both static and dynamic wettability of the latter samples showed a near-linear tendency with the increase of apparent part of the decorating NPs. Finally, the relationship between the wettability and NP apparent height (H_N) of the Cu NP decorated PMMA surfaces was theoretically explained by evaluating the wettability contribution of the nanomeniscus formed between the decorating NP and the flat substrate. In addition, the effect of the coverage (C_N) of NPs on wettability was also checked compared with experimental results and theoretical analysis. In summary, our results provide a comprehensive understanding of how nanostructure affects the wettability of the decorated surfaces and shed light on obtaining certain wettability through structuring the surface morphology.

ACKNOWLEDGMENTS

We thank Prof. F. Picchioni, and M. de Vries for their kindly offering the guidance and facilities for high-pressure CO_2 treatment. We would also like to acknowledge useful discussions with Prof. B. J. Kooi about the TEM characterizations. Moreover, we would like to acknowledge financial support from the China Scholarship Council (W.G.).

APPENDIX: PREPARATION METHODS AND CHARACTERIZATION

1. Fabrication of PMMA substrates, Cu NPs deposition, and high-pressure CO_2 assisted NP engulfment

PMMA films were prepared by drop casting a PMMA-chloroform solution (0.1 g/mL) onto silica wafers (1 cm × 1 cm). The PMMA we used is a commercial product labeled with "Diakon LG156", and the properties of the polymer are available on the website [50], and we suppose this PMMA is replaceable by the PMMA with other brands or molecular weights. Afterwards, the substrates were dried in air for 24 h and then annealed at 135 °C for 12 h, and slowly cooled down to room temperature within the furnace. Additionally, the thickness of PMMA films on the silica using the same method was measured by Liu *et al.* [31] to be around 50 μm, indicating that the PMMA films were thick enough for this work because this thickness is much larger than the diameter of the deposited Cu NPs.

The Cu NPs were deposited in a modified *Mantis Nanogen* 50 system on the PMMA substrates, with the Cu NPs having a native surface oxide layer. A TEM grid with a continuous carbon supporting film was put together with the PMMA substrates for subsequent TEM observations. Then the Cu NPs were deposited simultaneously on PMMA substrates and the TEM grids in the magnetron sputtering system to ensure that the NP distribution on the Cu NP/PMMA samples and the TEM grid are the same. Moreover, the size and coverage of the Cu NPs were controlled by the settings in the *Mantis Nanogen* 50 system. More details can be seen in our previous work [25].

Finally, the NPs/PMMA samples were placed inside a high-pressure vessel. The setup temperature was 40 °C, and the pressure of CO_2 was 58 bar. Moreover, the time span for the CO_2 treatment was controlled to generate samples with various morphologies. After each CO_2 treatment, the valve connecting the high-pressure vessel and the open air would be slowly opened releasing the CO_2 into the open air.

2. TEM, AFM, and SEM characterization

The morphology of the as-deposited NPs was characterized using a JEOL 2010 at an acceleration voltage of 200 kV to record the bright-field TEM images of the Cu NPs on the TEM grids. Furthermore, the AFM images were obtained by a Bruker Multimode 8 AFM using tapping mode with a silicon cantilever (HQ:NSC15/No Al) having a resonance frequency of 325 kHz and a spring constant of 40 N/m. Moreover, the apparent heights of individual NPs were analyzed based on the obtained AFM images. The method for deriving the apparent height of an individual isolated NP is shown in the Supplemental Material [38]. Finally, the morphology of the

NPs on silica was characterized using an FEI Nova NanoSEM 650 at an acceleration voltage of 5 kV to record the secondary electron images of the Cu NPs on the substrates.

3. Contact angle measurement

The CA measurements were performed using a Dataphysics OCA25 system. An automated syringe dropped 2-μL droplets of pure water (MilliQ) on the sample, where a camera recorded the pictures over several seconds. Immediately after the testing droplet was loaded onto the measured surface, the camera started to record the meniscus for 10 s and made the process as a video. Then the measured SCA was derived after "2 s" from the video, because the SCA is more "stable" after 2 s of the loading of the testing droplet [51]. The injecting/withdrawing speeds for advancing/receding contact angle measurements were both 0.2 μL/s, allowing the movement of the TPL steadily and smoothly. The drop shape was analyzed based on the form of an ideal sessile drop, for which the surface curvature results only from the force equilibrium between surface tension and weight of the liquid drop. The values of the contact angle were obtained *via* a fit using the Young-Laplace (YL) equation based on the shape analysis of a complete drop, and also compared to the results obtained from the geometrical CA analysis. For every sample, the CA measurements were repeated for several drops on different sample areas. In addition, the temperature was 20 °C, while the relative humidity was around 50%.

[1] W. Barthlott and C. Neinhuis, Purity of the sacred lotus, or escape from contamination in biological surfaces, Planta **202**, 1 (1997).

[2] S. S. Latthe, R. S. Sutar, V. S. Kodag, A. K. Bhosale, A. M. Kumar, K. Kumar Sadasivuni, R. Xing, and S. Liu, Self – cleaning superhydrophobic coatings: Potential industrial applications, Prog. Org. Coat. **128**, 52 (2019).

[3] D. Daniel, A. Y. T. Chia, L. C. H. Moh, R. Liu, X. Q. Koh, X. Zhang, and N. Tomczak, Hydration lubrication of polyzwitterionic brushes leads to nearly friction- and adhesion-free droplet motion, Commun. Phys. **2**, 105 (2019).

[4] L. Feng, Y. Zhang, J. Xi, Y. Zhu, N. Wang, F. Xia, and L. Jiang, Petal effect: A superhydrophobic state with high adhesive force, Langmuir **24**, 4114 (2008).

[5] F.-M. Chang, S.-J. Hong, Y.-J. Sheng, and H.-K. Tsao, High contact angle hysteresis of superhydrophobic surfaces: Hydrophobic defects, Appl. Phys. Lett. **95**, 064102 (2009).

[6] B. Bhushan and E. K. Her, Fabrication of superhydrophobic surfaces with high and low adhesion inspired from rose petal, Langmuir **26**, 8207 (2010).

[7] X. Hong, X. Gao, and L. Jiang, Application of superhydrophobic surface with high adhesive force in no lost transport of superparamagnetic microdroplet, J. Am. Chem. Soc. **129**, 1478 (2007).

[8] Y. Chen, Y. Jie, J. Wang, J. Ma, X. Jia, W. Dou, and X. Cao, Triboelectrification on natural rose petal for harvesting environmental mechanical energy, Nano Energy **50**, 441 (2018).

[9] R. N. Wenzel, Resistance of solid surfaces to wetting by water, Ind. Eng. Chem **28**, 988 (1936).

[10] A. B. D. Cassie and S. Baxter, Wettability of porous surfaces, Trans. Faraday Soc. **40**, 546 (1944).

[11] L. Jiang, Y. Zhao, and J. Zhai, A lotus-leaf-like superhydrophobic surface: A porous microsphere/nanofiber composite film prepared by electrohydrodynamics, Angew. Chem. **116**, 4438 (2004).

[12] A. Marmur, The lotus effect: Superhydrophobicity and metastability, Langmuir **20**, 3517 (2004).

[13] N. A. Patankar, Mimicking the lotus effect: Influence of double roughness structures and slender pillars, Langmuir **20**, 8209 (2004).

[14] D. C. Pease, The significance of the contact angle in relation to the solid surface, J. Phys. Chem. **49**, 107 (1945).

[15] E. Schäffer and P.-Z. Wong, Contact line dynamics near the pinning threshold: A capillary rise and fall experiment, Phys. Rev. E **61**, 5257 (2000).

[16] S. M. M. Ramos, E. Charlaix, A. Benyagoub, and M. Toulemonde, Wetting on nanorough surfaces, Phys. Rev. E **67**, 031604 (2003).

[17] L. Gao and T. J. McCarthy, How Wenzel and Cassie were wrong, Langmuir **23**, 3762 (2007).

[18] P. S. H. Forsberg, C. Priest, M. Brinkmann, R. Sedev, and J. Ralston, Contact line pinning on microstructured surfaces for liquids in the Wenzel state, Langmuir **26**, 860 (2010).

[19] T. Ondarçuhu and A. Piednoir, Pinning of a contact line on nanometric steps during the dewetting of a terraced substrate, Nano Lett. **5**, 1744 (2005).

[20] W. Guo, B. Chen, V. L. Do, G. H. ten Brink, B. J. Kooi, V. B. Svetovoy, and G. Palasantzas, Effect of airborne hydrocarbons on the wettability of phase change nanoparticle decorated surfaces, ACS Nano **13**, 13430 (2019).

[21] F.-C. Wang and H.-A. Wu, Pinning and depinning mechanism of the contact line during evaporation of nano-droplets sessile on textured surfaces, Soft Matter **9**, 5703 (2013).

[22] Y. Li, H. Wu, and F. Wang, Effect of a single nanoparticle on the contact line motion, Langmuir **32**, 12676 (2016).

[23] Y. Lu, S. Sathasivam, J. Song, C. R. Crick, C. J. Carmalt, and I. P. Parkin, Robust self-cleaning surfaces that function when exposed to either air or oil, Science **347**, 1132 (2015).

[24] G. H. ten Brink, N. Foley, D. Zwaan, B. J. Kooi, and G. Palasantzas, Roughness controlled superhydrophobicity on single nanometer length scale with metal nanoparticles, RSC Adv. **5**, 28696 (2015).

[25] G. H. ten Brink, G. Krishnan, B. J. Kooi, and G. Palasantzas, Copper nanoparticle formation in a reducing gas environment, J. Appl. Phys. **116**, 104302 (2014).

[26] J. H. Teichroeb and J. A. Forrest, Direct Imaging of Nanoparticle Embedding to Probe Viscoelasticity of Polymer Surfaces, Phys. Rev. Lett. **91**, 016104 (2003).

[27] W. S. Tan, Y. Du, L. E. Luna, Y. Khitass, R. E. Cohen, and M. F. Rubner, Templated nanopores for robust functional surface porosity in poly(methyl methacrylate), Langmuir **28**, 13496 (2012).

[28] M. Qu, J. S. Meth, G. S. Blackman, G. M. Cohen, K. G. Sharp, and K. J. V. Vliet, Tailoring and probing particle–polymer interactions in pmma/silica nanocomposites, Soft Matter **7**, 8401 (2011).

[29] J. Yang, C. Liu, Y. Yang, B. Zhu, L. J. Lee, H. Chen, and Y. C. Jean, Analysis of polystyrene surface properties on thin film bonding under carbon dioxide pressure using nanoparticle embedding technique, J. Polym. Sci. Part B Polym. Phys. **47**, 1535 (2009).

[30] Q. Yang, Q. Xu, and K. Loos, Enhanced polystyrene surface mobility under carbon dioxide at low temperature for nanoparticle embedding control, Macromolecules **48**, 1786 (2015).

[31] S. Liu, A. Pandey, J. Duvigneau, J. Vancso, and J. H. Snoeijer, Size-dependent submerging of nanoparticles in polymer melts: Effect of line tension, Macromolecules **51**, 2411 (2018).

[32] R. Seemann, S. Herminghaus, and K. Jacobs, Gaining control of pattern formation of dewetting liquid films, J. Phys.: Condens. Matter **13**, 4925 (2001).

[33] C. Jai, Aimé, D. Mariolle, R. Boisgard, and F. Bertin, Wetting an oscillating nanoneedle to image an air−liquid interface at the nanometer scale: Dynamical behavior of a nanomeniscus, Nano Lett. **6**, 2554 (2006).

[34] J. Kim, D. Won, B. Sung, and W. Jhe, Observation of universal solidification in the elongated water nanomeniscus, J. Phys. Chem. Lett. **5**, 737 (2014).

[35] H. R. Eisenberg and D. Kandel, Wetting Layer Thickness and Early Evolution of Epitaxially Strained Thin Films, Phys. Rev. Lett. **85**, 1286 (2000).

[36] H. R. Eisenberg and D. Kandel, Origin and properties of the wetting layer and early evolution of epitaxially strained thin films, Phys. Rev. B **66**, 155429 (2002).

[37] Q. Yuan and Y.-P. Zhao, Precursor Film in Dynamic Wetting, Electrowetting, and Electro-Elasto-Capillarity, Phys. Rev. Lett. **104**, 246101 (2010).

[38] See Supplemental Material at http://link.aps.org/supplemental/10.1103/PhysRevMaterials.5.015604 for further information about sample storage condition, measurements, and experimental results.

[39] L. Sawyer, D. T. Grubb, and G. F. Meyers, *Polymer Microscopy* (Springer Science & Business Media, New York, 2008).

[40] C. A. Goss, J. C. Brumfield, E. A. Irene, and R. W. Murray, Imaging and modification of gold(111) monatomic steps with atomic force microscopy, Langmuir **9**, 2986 (1993).

[41] D. Tranchida, S. Piccarolo, and R. A. C. Deblieck, Some experimental issues of afm tip blind estimation: The effect of noise and resolution, Meas. Sci. Technol. **17**, 2630 (2006).

[42] R. García and R. Pérez, Dynamic atomic force microscopy methods, Surf. Sci. Rep. **47**, 197 (2002).

[43] A. N. Frumkin, On wetting and sticking phenomena, Z. Phys. Chem. (USSR) **12**, 337 (1938).

[44] B. V. Derjaguin, Theory of capillary condensation and other capillary phenomena accounting for the disjoining pressure of polymolecular liquid films, Acta Physicochim. URSS **12**, 181 (1940).

[45] B. V. Derjaguin, N. V. Churaev, and V. M. Muller, *Surfaces Forces* (Consultant Bureau, New York,1987).

[46] N. V. Churaev, Contact angles and surface forces, Adv. Colloid Interface Sci. **58**, 87 (1995).

[47] L. Boinovich and A. Emelyanenko, The prediction of wettability of curved surfaces on the basis of the isotherms of the disjoining pressure, Colloids Surf., A **383**, 10 (2011).

[48] A. I. Rusanov, A. K. Shchekin, and V. B. Varshavskii, Three-dimensional aspect of the surface tension: An approach based on the total pressure tensor, Colloid J **63**, 11 (2001).

[49] A. I. Rusanov and A. K. Shchekin, Local mechanical equilibrium conditions for interfaces and thin films of arbitrary shape, Mol. Phys. **103**, 2911 (2005).

[50] Lucite international Diakon® LG156 acrylic bead polymer, high transparency, http://www.matweb.com/search/datasheet.aspx?matguid=b2f3a43118304a899bf1293c26bbe83b&n=1.

[51] G. H. ten Brink, P. J. van het Hof, B. Chen, M. Sedighi, B. J. Kooi, and G. Palasantzas, Control surface wettability with nanoparticles from phase-change materials, Appl. Phys. Lett. **109**, 234102 (2016).